Molecular Catalysis 445 (2018) 257–268

Contents lists available at ScienceDirect

Molecular Catalysis

journal homepage: www.elsevier.com/locate/mcat

Graphene supported Cu nanoparticles as catalysts for the synthesis of dimethyl carbonate: Effect of carbon black intercalation

Ruina Shi, Meijiao Ren, Haixia Li, Jinxian Zhao, Shusen Liu, Zhong Li, Jun Ren*

Key Laboratory of Coal Science and Technology, Taiyuan University of Technology, Ministry of Education and Shanxi Province, Taiyuan 030024, China

ARTICLE INFO

Article history:
Received 27 June 2017
Received in revised form 2 December 2017
Accepted 3 December 2017

Keywords:
Reduced graphene oxide
Intercalation
Carbon black
Oxygen containing groups
Dimethyl carbonate

ABSTRACT

Reduced graphene oxide (rGO) intercalated with a carbon black (CB) supported copper catalyst (Cu/rGO-CB) was employed in the synthesis of dimethyl carbonate (DMC) via liquid-phase oxidative carbonylation of methanol. The conversion of methanol and the space-time yield of DMC (STY_{DMC}) over Cu/rGO-CB reached 5.6% and 2757 mg/(g h), higher than over a Cu/rGO catalyst, 4.7% and 2334 mg/(g h), respectively. The characterization indicates that CB particles, acting as spacers, ensured the high utilization of graphene layers and enhanced the interaction between Cu and the support, and the oxygen containing groups on the surface of CB play an important role in stabilizing Cu clusters. In comparison with Cu/rGO, the loss of copper concentration in Cu/rGO-CB is significantly decreased, from 15.37% to 1.96%. Catalyst reusability tests show that Cu/rGO-CB could be reused five times without almost any catalytic activity loss, implying distinct enhanced catalytic stability compared to the Cu/rGO catalyst.

1. Introduction

The research and development of dimethyl carbonate (DMC) have recently received significant attention because of its low toxicity and high biodegradability, which make it a promising environmentally benign compound and a safer alternative to poisonous dimethyl sulfate and phosgene [1,2]. The direct oxidative carbonylation of methanol using CuCl as a catalyst in the liquid phase is one of the most promising commercial processes for the production of DMC. Nevertheless, severe catalyst deactivation is frequently observed. The short lifespan of conventional catalysts inhibits their applications because of the loss of active species under elevated reaction conditions. In fact, in addition to the DMC synthesis, many liquid phase reactions are also faced with this problem [3–5], such as biorefineries [6], ammoxidation [7], the hydrolysis of cellulose [8] and dehydration of carbohydrates [9]. In summary, the loss of active species is a common and urgent problem in liquid phase reactions.

In order to solve this problem, a variety of catalysts have been explored for the synthesis of DMC. Li et al. [10] found that the addition of 1, 10-phenanthroline, used as a ligand, could dramatically enhance the catalytic performance of CuCl and effectively inhibit the corrosion of the reaction system. However, the recovery and reuse of the efficient homogeneous catalyst, CuCl/Phen, are not so easy. Liu [11] and coworkers first demonstrated that ionic liquid-mediated Cu salts are an efficient catalyst system for oxidative carbonylation of methanol to produce DMC. Furthermore, the catalytic system can be reused for at least five recycles with only a slight decrease in activity. Meanwhile, different materials have been employed to stabilize the active Cu species, such as SBA-15 [12], SiO_2-TiO_2 [13], zeolite [14], activated carbon (AC) [15,16] and carbon hollow spheres [17].

In our previous study [17], Cu@carbon york-shell nanocomposite exhibited promising catalytic property and stability towards DMC synthesis, which could be attributed to a spatially confined effect on the enhanced immobilization of Cu nanoparticles (NPs). Furthermore, Li et al. [15] investigated the catalytic properties of Cu/AC catalysts in DMC synthesis. It was indicated that the increased surface oxygenated groups have a significant influence on both the dispersion and valence distributions of Cu species, as well as the catalytic performance of the resulting Cu-based catalysts. In conclusion, the modification of the spatial structure or surface chemistry can be an effective method to improve the catalytic performance of carbon-supported Cu catalysts.

Recently, a variety of carbon materials representing a unique family of supports that possess unique structures and properties, including highly porous frameworks and enhanced stability in both acidic and basic media, have been synthesized successfully, such as AC, carbon nanotubes, graphite, diamond, fullerenes, carbon black (CB) and graphene [18–20]. Among all carbon allotropes, graphene,

* Corresponding author at: No. 79 Yingze West Street, Taiyuan 030024, China.
E-mail addresses: renjun@tyut.edu.cn, 286945754@qq.com (J. Ren).

https://doi.org/10.1016/j.mcat.2017.12.002
2468-8231/

a two-dimensional (2D) single-layer sheet of graphite comprising a planar hexagonal lattice of carbon atoms [21], exhibiting considerable potential as excellent supporting material for various heterogeneous catalysts since it affords high theoretical specific surface area of about 2600 $m^2 g^{-1}$, has attracted increasing attention [22–24]. Generally, graphene samples with two or more layers have being investigated with equal interest [25]. Notably, the high surface area of graphene materials does not depend on the distribution of pores in solid state, but comes from the interconnected open channels between graphene layers distributed in a 2D architecture [26]. In addition, due to the inevitable carbon vacancy defects and functional groups presented in chemically derived graphene, metal ions can be adsorbed and intercalated into graphene sheets to form thermally stable composite materials. More importantly, usage of the support can increase the stability of the catalyst, optimize the dispersion of the active components of the catalyst and provide important chemical, mechanical, thermal and morphological properties. Fu et al. [27] reported that interfaces between graphitic overlayers and metal surfaces act as 2D confined nanoreactors, in which catalytic reactions are promoted. This finding contrasts with the conventional knowledge that graphitic carbon poisons a catalyst surface but opens up an avenue to enhance catalytic performance through the coating of metal catalysts with controlled graphitic covers.

Tremendous progress has so far been achieved in composite materials. CB, which has a large specific surface area, cheap price and can form an open space network channel, is recognized as a promising candidate as a carbon support material. Flexible reduced graphene oxide (rGO)-CB hybrid films with different CB contents have been prepared by a simple vacuum filtration method. The CB particles between the graphene layers act as spacers that prevent the restacking of graphene layers and inhibit the agglomeration of graphene sheets [28]. Fan et al. [26] prepared rGO-CB pulverous composites by ultrasonication and in-situ reduction methods. The as-fabricated rGO-CB powder-composite electrode shows enhanced capacitance and rate capability. Currently, the reported rGOCB material has only been used in electrochemistry. It is desirable to develop a new-type of supported-catalysts for the synthesis of DMC to take full advantage of rGO-CB. Therefore, extensive efforts have been exerted to develop such catalysts in our work.

It is well known that metal oxide (or metal hydroxide) NPs can also act as spacers in the interlayers of graphene sheets to prevent aggregation, thereby increasing the interplanar spacing and contact area with the reactant [29,30]. Various strategies have been developed for the synthesis of metal or metal oxide-embedded graphene composites, including chemical methods [31], photo-synthesis [32] and microwave-assisted synthesis [33,34]. Several studies have addressed the applications of graphene for various catalytic reactions. Most of the reported graphene-based catalysts exhibit high activity and stability [35]. Some studies [36] have demonstrated that the catalytic activity can be influenced by the metal active site supported on graphene. Meanwhile, the oxygen functional groups on the surface of the support also have an effect on the catalyst structure and catalytic activity [37].

In our work, an innovative and economical approach has been employed for synthesizing a Cu/rGO-CB catalyst by a simple ultrasonication and vacuum filtration process. The synthetic effects of rGO sheets and CB lead to a large accessible surface area for the Cu NPs. As spacers, CB particles can not only increase the distance between the graphene sheets, but also provide rapid diffusion paths for reactants in double-layer films. Furthermore, CB can also provide adsorption sites for Cu NPs. As a result, the CB spacers ensure high specific surface utilization of graphene layers, as well as the open nanochannels provided by the three-dimensional rGO-CB hybrid material. Using catalyst characterization, the interaction between Cu NPs and graphene, as well as CB, has been investigated, which is also useful for understanding the interaction between Cu NPs and the support. The properties of the Cu/rGO-CB catalyst were evaluated by liquid-phase oxidative carbonylation of methanol, with excellent cycling stability exhibited.

2. Experimental

2.1. Materials

GO was obtained from Jinneng Co., Ltd. of Institute of the Coal Chemistry, Chinese Academy of Sciences (Taiyuan, China). CB was obtained as a commercial product from the Xinhua chemical plant (Taiyuan, China). Copper nitrate ($Cu(NO_3)_2{\cdot}3H_2O$) was purchased from Sinopharm Chemical Reagent Co., Ltd. Methanol, ethanol, hydrazine and *N*,*N*-dimethylformamide (DMF) were purchased from Sinopharm Chemical Reagent Co. Ltd. (Beijing, China). Hexadecyltrimethyl-ammonium Bromide (CTAB) was obtained from Shanghai Nuotai Chemical Co., Ltd. All chemicals were of analytical grade and were used without any further purification.

2.2. Cu/rGO-CB and Cu/rGO nanocomposite synthesis

For the preparation of the Cu/rGO-CB catalyst, GO (200 mg) was first mixed with 200 mL of absolute ethanol under ultrasonic sonication at room temperature for 2 h. Meanwhile, 50 mg of CB (>200 mesh) was dispersed into 200 mL of absolute DMF under ultrasonic sonication for 1 h. Subsequently, the as-prepared CB dispersions with a volume of 5 mL were diluted with 50 mL of DMF. Then, the two suspensions were mixed and kept under ultrasonic sonication for another 2 h. Next, the mixture was magnetically stirred to form a homogeneous mixture using a water bath at room temperature. In the subsequent step, 80 mg of $Cu(NO_3)_2{\cdot}3H_2O$ and a small quantity of CTAB, acting as a dispersing agent, were added to the mixture, while maintaining a vigorous agitation for 3 h at 90 °C. Ultimately, 0.5 mL of hydrazine (50 wt.% in water) was added to the mixture dropwise. The solution turned from deep orange to black within minutes, followed by the appearance of a black precipitate to yield Cu/rGO-CB composites. Finally, the solid was filtered and washed several times with distilled water and alcohol, then dried at 100 °C for 12 h in a vacuum oven. Hitherto, the resulting sample labeled as Cu/rGO-CB was prepared. Similarly, as a comparison, Cu/rGO was synthesized without CB. Scheme 1 shows the fabrication scheme for the Cu/rGO-CB nanocomposite.

2.3. Catalyst characterization techniques

The analysis of the crystal structure and phase composition of the catalyst was completed using X-ray diffraction (XRD) on a Rigaku D/Max 2500 system with a Cu Kα radiation (λ = 1.54056 Å) and a graphite monochromator. The voltage and current of the measurements were operated at 40 kV and 100 mA, and the scanning speed was 8°/min at a scanning region of 5–85°. The crystallite size of Cu metal for the catalysts was calculated using the Scherrer equation.

The Cu K-edge X-ray absorption fine structure (XAFS) analysis of the catalysts was performed by the Soft X-ray Microcharacterization Beamline (SXRMB) of the Canadian Light Source. SXRMB is a medium energy beamline with a range of 1.7–10 keV. The monochromator of the beamline consists of two pairs of crystals, InSbC (111) and Si (111).

A Fourier transform infrared (FT-IR) spectroscopy analysis was conducted to explore the change of oxygen-containing functional groups on GO after reduction by hydrazine using a FT-IR spectrometer (Nicolet Nexus 470, Thermo Nicolet, Madison, WL USA) in the range of 500–4000 cm^{-1}.

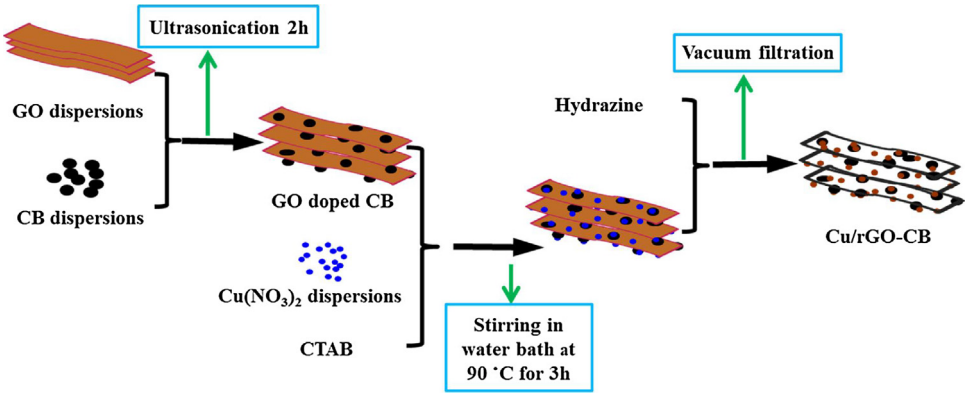

Scheme 1. The fabrication scheme for the Cu/rGO-CB nanocomposite.

An X-ray photoelectron spectroscopy (XPS) analysis (PHI1600 ESCA System, PERKIN ELMER, Nowalk, CT, USA) was carried out using Al Ka radiation (hn ¼ 1486.6 eV) and the XPS spectra were fitted using the XPS peak 4.1 software, in which a Shirley background was used to perform curve fitting and to calculate the atomic concentrations.

The particle size and morphology of the as-prepared and heat treated graphene nanocomposites were investigated using a JEM-6700F scanning electron microscope (SEM, JEOL, Tokyo, Japan). The sample was immobilized on a Cu substrate by conductive adhesives without further processing. The particle size analysis was performed using image particle size analysis software.

The microscopic features, such as the surface morphology and dispersion of the active components of the samples, were observed using transmission electron microscopy (TEM) (JEM-2010F, JEOL). The samples were adequately dispersed in absolute ethyl alcohol through an ultrasonic method. After a period time, the samples can be made by dripping the upper solution to the brass or micro grid.

The specific surface area and pore size distribution of the samples by the N_2 adsorption-desorption characterization were investigated at −196 °C on a Micromeritics 3H-2000PS2 (BeiShiDe Instruments S&T. (Beijing) Co., Ltd) specific surface area and pore size analysis instrument. Prior to the measurement, the samples were pretreated by degassing at 300 °C under a vacuum for 3 h. The specific surface areas of the samples were calculated by the Brunauer-Emmett-Teller (BET) method and the pore volume and pore size distribution of the samples were obtained from the Barrett-Joyner-Halenda (BJH) method.

CO temperature-programmed desorption (CO-TPD) was performed using a Finsore-3010 apparatus (FINETEC Zhejiang China). First, the sample (50 mg) was pretreated under a stream of He. Then, the sample was cooled to room temperature and saturated with CO. After removing the physically adsorbed CO by flushing with He, the sample was heated to 300 °C at a heating rate of 10 °C/min in He flow.

2.4. Catalytic tests

The reaction for the direct synthesis of DMC by liquid-phase oxidative carbonylation of methanol was carried out in a 25 mL stainless steel high pressure reactor (model SLM25, Beijing Century Senlang experimental apparatus Co., Ltd) equipped with a thermocouple (type J), heating mantle and controller (model 4848). A volume of 10 mL of methanol was added to 0.15 g of the Cu/rGO-CB catalyst in a typical process. Then, CO and O_2 were injected at a specified pressure of 2:1 to the reactor. The reactor was heated to the required temperature (120 °C) and continuously stirred for 1.5 h. After the reaction, the reactor was cooled down to room temperature and the reaction mixture was filtered by centrifugation. The concentrations of DMC, methanol, methyl formate (MF) and dimethoxymethane (DMM) were analyzed using a GC-950 gas chromatograph (Shanghai Haixin, China) equipped with a flame ionization detector.

Table 1
Surface and physical properties of Cu/rGO and Cu/rGO-CB catalysts.

Catalysts	N_2 sorption analysis		
	S_{BET}[a] ($m^2\ g^{-1}$)	Vt[b] ($cm^3\ g^{-1}$)	D_p (nm)
Cu/rGO	245.9	0.28	3.90
Cu/rGO-CB	415.3	1.03	4.04

[a] BET specific surface areas determined from the linear part of the BET equation (P/P_0 = 0.05–0.25).
[b] Total pore volumes obtained at P/P_0 = 0.99.

3. Results and discussion

3.1. Catalyst characterization

3.1.1. N_2 adsorption

Furthermore, the specific surface areas of the Cu/rGO and Cu/rGO-CB composites calculated by the BET method are 245.9 and 415.3 m^2/g, respectively. This means that CB particles as nanoscale spacers can effectively decrease the stacking of graphene, resulting in the high utilization of graphene layers. Table 1 lists the porosity characteristics of the two catalysts. Comparing the non-intercalated materials, the BET specific surface area increased with as the intercalation of CB particles, accompanied by a slight change in pore volume. This can be explained by the fact that the substitution of CB tends to create more defects in the structure, thereby increasing the porosity of highly intercalated materials. In addition, the nitrogen adsorption and desorption isotherms (according to the IUPAC classification) presented a H3 hysteresis loop, as shown in Fig. 1, suggesting that slit-shaped apertures existed between parallel graphene layers [38] and that CB can effectively prevent the reunion of graphene layers to further provide more open reaction spaces for reactants. This result is in agreement with the TEM analysis.

3.1.2. XRD

Fig. 2 demonstrates the XRD patterns of GO, rGO, CB, rGO-CB, Cu/rGO and Cu/rGO-CB. It is clear that only one obvious sharp diffraction peak at 2θ = 12.0°, corresponding to the diffraction of the (001) plane, was detected to GO, which demonstrates the high crystallinity of this material [39]. This distance between layers (d-spacing) is typically 0.75 nm larger than the 0.34 nm for graphene, indicating the presence of abundant oxygen-containing groups

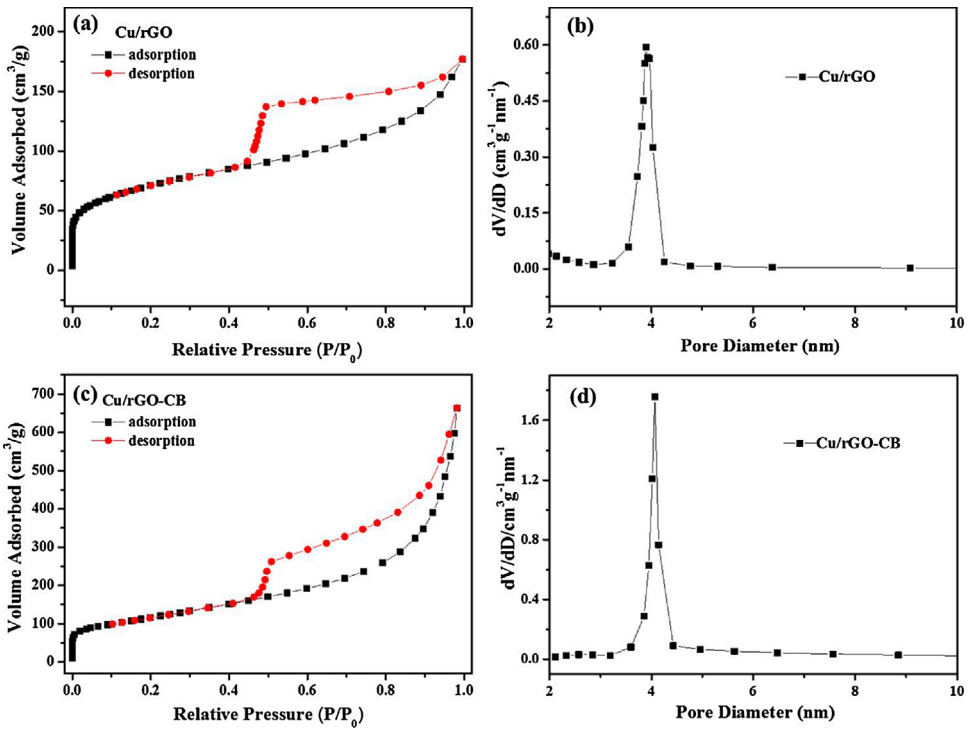

Fig. 1. N_2 adsorption–desorption isotherms of (a) Cu/rGO and (c) Cu/rGO-CB; pore size distributions of (b) Cu/rGO and (d) Cu/rGO-CB.

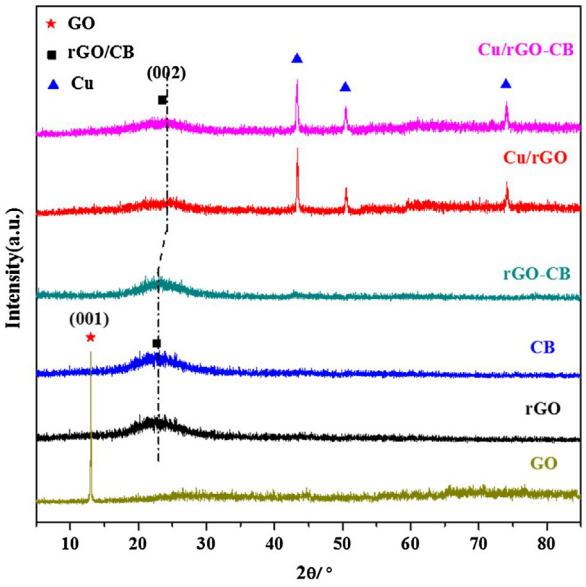

Fig. 2. XRD patterns of GO, rGO, CB, rGO-CB, Cu/rGO and Cu/rGO-CB.

between the graphene layers. However, this peak disappeared and the (002) diffraction peak of graphite appeared at $2\theta = 25.1^\circ$ for other rGO-based materials, which is an indication that GO has been reduced to graphene by hydrazine, and that the regular stack of GO has been broken [40]. However, for the Cu-based catalysts, Cu/rGO and Cu/rGO-CB, the peak position of rGO moves to the right, showing that Cu species had a strong interaction with the graphene after reduction by hydrazine and shortened layer spacing. In addition, the Cu peaks centered at 43.3°, 50.5° and 74.2°, which are assigned to the (111), (200), and (220) planes of face-centered cubic structure of Cu (JCPDS 65-9026), suggests the occurrence of reduction reactions. Meanwhile, note that the full width at half maximum of the Cu peaks of Cu/rGO-CB is decreased smaller than Cu/rGO, illustrating that Cu particles with smaller sizes are well dispersed on the surface of the supports [41]. The average outside diameters of Cu/rGO and Cu/rGO-CB are 39.8 and 20.3 nm, respectively, calculated using the Debye–Scherrer equation. Therefore, the XRD pattern indicates that CB as a dispersing medium can effectively prevent the aggregation and restacking of graphene sheets and thus improves the attachment of Cu NPs on the surface of graphene sheets during the composite preparation [42].

3.1.3. FT-IR

FT-IR spectroscopy is a useful non-destructive tool for characterizing oxygen-containing functional groups on the support surface and carbonaceous materials, particularly for distinguishing ordered and disordered carbon structures. Fig. 3 compares the FT-IR spectra of GO, rGO, rGO-CB, Cu/rGO and Cu/rGO-CB. The GO spectrum shows the presence of various oxygen-containing groups compared to rGO. In particular, in the vicinity of 3400 and 1040 cm^{-1}, there was a large and broad peak, which was attributed to the O—H stretching vibration peak of the carboxyl group. These results agree with those reported in the literature [39,43]. In addition, the peaks around 1733, 1408 and 1050 cm^{-1} are assigned to C=O, O—H and C—O—C vibrations, respectively [44,45]. Most contributions from oxygen-containing groups decrease or disappear after reduction by hydrazine, which demonstrates that GO has been reduced to rGO. The minor changes of the surface groups of the support after reduction are clearly shown in Fig. 3. The oxygen-containing functional groups were severely reduced after reduction by hydrazine, indicating that the reduction of hydrazine to GO is effective, but there are still some residual oxygen containing functional groups, which are beneficial for the combination of Cu species in turn. The result is further demonstrated in section 3.1.4. For the Cu/rGO-CB catalyst, the original carbonyl stretching vibration peak located at 1733 cm^{-1} shifted to 1687 cm^{-1} after loading Cu, which further indicated that Cu species had a strong interaction with support, resulting in a bathochromic shift of the infrared spectra of 46 cm^{-1}. This conclusion is also supported by the XRD results.

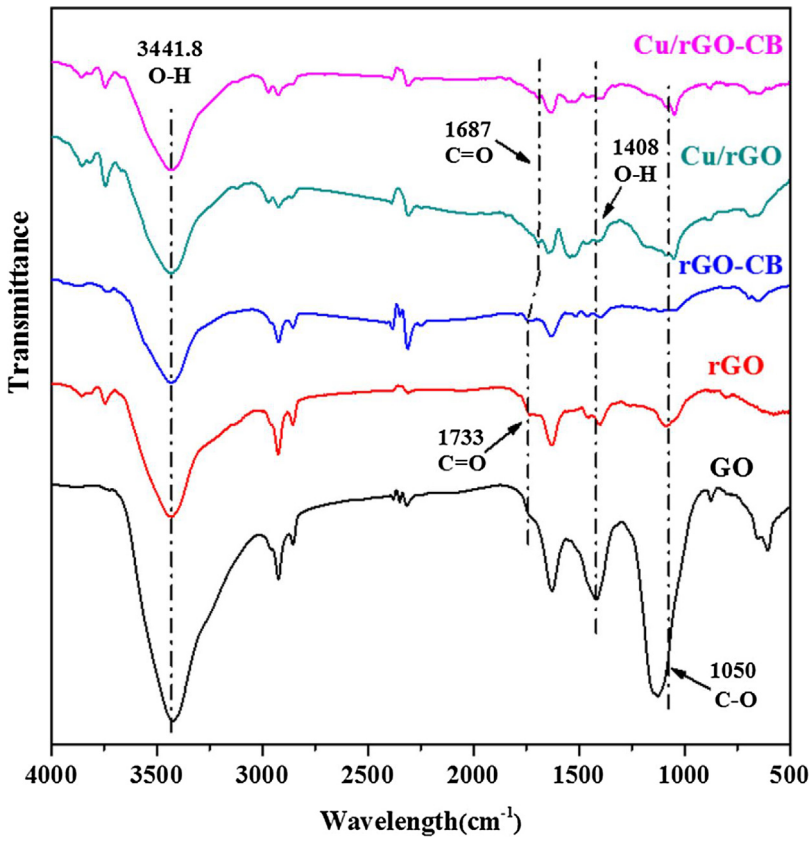

Fig. 3. FT-IR spectra of GO, rGO-CB, rGO, Cu/rGO and Cu/rGO-CB.

3.1.4. XPS

To investigate the compositional atomic concentrations of GO, rGO and rGO-CB, XPS analysis was used. The high-resolution C 1s and O 1s XPS spectra are presented in Figs. 4(a) and (b), respectively. The deconvolution of C 1s (Fig. 4(a)) spectra reveals the presence of three peaks: the nonoxygenated ring C (284.6 eV), the C in C—OH bonds (286.4 eV) and C in C═O (287.8 eV) [46,47]. The structural models of GO also contains an epoxide group (C—O—C), which should have a C1 s binding energy similar to C—OH. Although the C 1s XPS spectra of the rGO and rGO-CB (Fig. 4(a)) also exhibit these same oxygen-containing functionalities, their peak intensities are much weaker compared to GO. Moreover, we can found that the rGO peak intensities at 286.4 and 287.8 eV are weaker than those in rGO-CB, which means compared to rGO, the rGO-CB has more oxygen functional groups. The O 1s spectra are shown in Fig. 4(b), and the asymmetric peak around 533 eV is similar to that observed in GO [39] and CB [48]. The deconvolution of the O 1s spectra reveals the presence of three peaks: oxygen singly bound to carbon (C—O), near 531.3 eV; oxygen doubly bound to carbon in carbonyl (C═O), around 532.6 eV; and oxygen doubly bound to carbon in carboxylate (O═C—O), near 533.1 eV [49]. The comprehensive results of the C 1s and O 1s XPS spectra reveal that part of the carbonyl and other oxygen functional groups are removed during the hydrogen reduction, while the other oxygen groups remaining on the graphene may reconstruct with the Cu NPs, leading to the formation of Cu^0 [26].

To monitor the surface Cu components of the catalysts during the reaction, the XPS results for fresh and used catalyst samples are reported in Fig. 5. The Cu $2p_{3/2}$ XPS spectra of the fresh Cu/rGO and Cu/rGO-CB catalysts are shown in Fig. 5(a) and (b). The Cu $2p_{3/2}$ XPS spectra of the used Cu/rGO and Cu/rGO-CB catalysts are shown in Fig. 5(c) and (d), respectively. Generally, $Cu2p_{3/2}$ spectra can be divided into two peaks corresponding to Cu^{2+} and ($Cu^+ + Cu^0$) for the sample. The binding energy at 934.5 eV has contributions from Cu^{2+}, and that at 932.5 eV was ($Cu^0 + Cu^+$) [15,50]. As shown in Figs. 5(a) and (b), we can see that $Cu(NO_3)_2$ has been reduced to ($Cu^0 + Cu^+$) by hydrazine. Furthermore, the binding energy for Cu^0 and Cu^+ is similar meaning that in order to see the difference between Cu^0 and Cu^+, Cu LMM XAES spectra need to be acquired. In Fig. 5(e–h), the kinetic energies at 917.0 and 915.5 eV correspond to Cu^0 and Cu^+, respectively. The surface Cu species counts of catalysts are listed in Table 2. This conclusion is also supported by the XRD patterns discussed above [51].

The valence of copper species plays an important role in catalytic performance, while it's controversial about which is most active species. Ma et al. [52,53] and Erdőhelyi et al. [54] believed that Cu(I) species was the best catalytic active center among the copper species. While our previous studies [55] displayed that the catalytic activity follows the order: Cu(0) > Cu(I) > Cu(II). In fact, there is subtle balance among Cu(0), Cu(I), and Cu(II) is also possible. In this paper, it is interesting to find that the ratio of ($Cu^0 + Cu^+$)/Cu^{2+} increases after intercalation with CB from Table 2. The insertion of CB provides more coalescent sites for active species, and thus improves the catalytic activity. Moreover, the XPS of used Cu/rGO and Cu/rGO-CB (Fig. 5 and Table 2) indicated that the deactivation of the catalyst can be attributed to the oxidation of Cu^0. Compared to Cu/rGO, ($Cu^0 + Cu^+$)/Cu^{2+} ratio of Cu/rGO-CB slightly decrease after five consecutive runs, indicating that the transformation of Cu^0 and Cu^+ to Cu^{2+} became much more difficult by intercalate CB. It can be deduced that Cu/rGO-CB catalyst has better oxidation resistance properties. In addition, the Cu contents of catalysts are also shown in Table 2. It can be seen from the XPS results that Cu particles supported on rGO-CB are more stable than those supported on rGO, which is attributed to the stronger interaction between Cu parti-

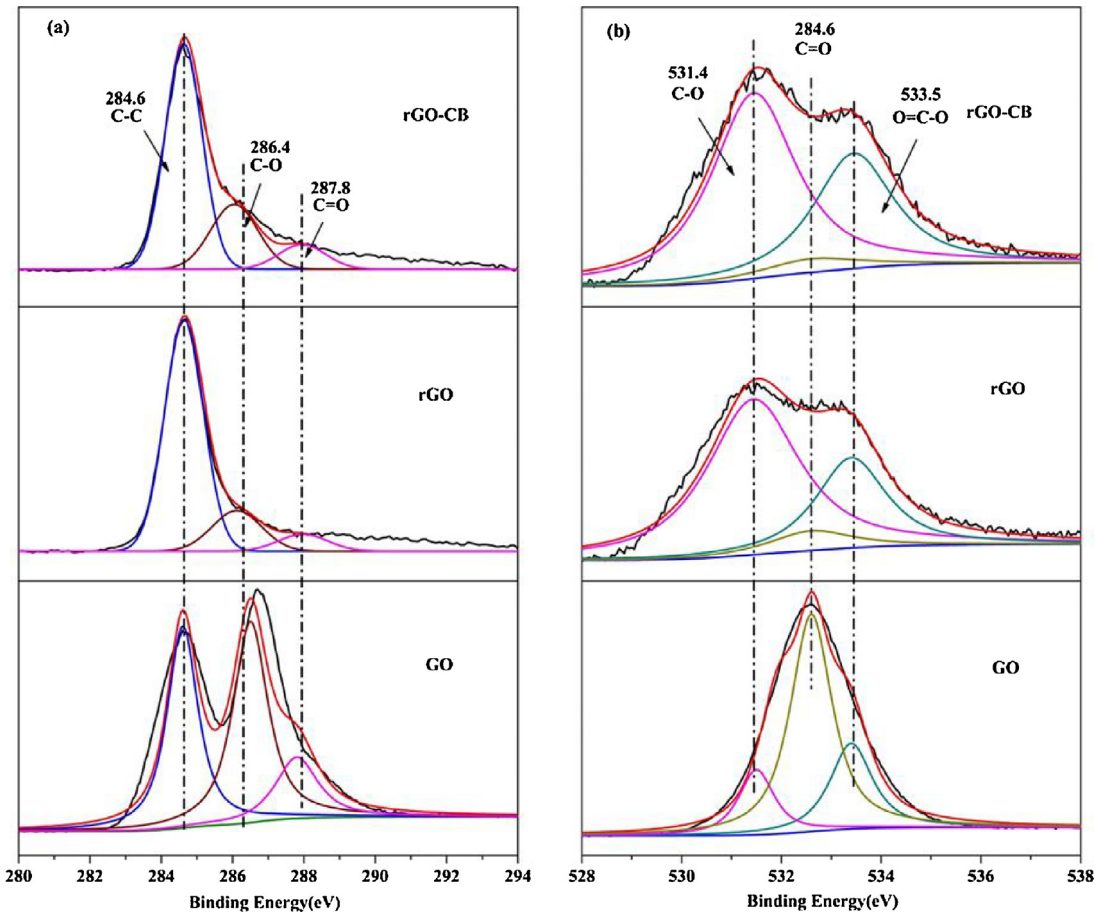

Fig. 4. XPS C 1s (a), O 1s (b) spectra of GO, rGO, CB and rGO-CB.

Table 2
Analysis of Cu LMM Auger spectra of Cu/rGO and Cu/rGO-CB.

Catalysts	Cu wt.% [a]	Cu wt.% [b]	$(Cu^0 + Cu^+)/Cu^{2+}$	Cu^0/Cu^+
Fresh Cu/rGO	6.57	6.14	0.74	1.02
Used Cu/rGO	5.56	5.06	0.49	0.81
Fresh Cu/rGO-CB	7.12	6.62	2.98	0.63
Used Cu/rGO-CB	6.98	6.51	2.83	0.60

[a] Determined from atomic absorption spectrometry (AAS).
[b] Determined from XPS analysis.

cles and rGO-CB. For Cu/rGO-CB, the Cu content is 6.51% after reuse five times, which is similar to the fresh catalyst (6.62%).

3.1.5. XAFS

To further investigate the structural and electronic differences in the as-synthesized samples, the normalized Cu K-edge X-ray absorption near-edge structure (XANES) spectra were collected and are presented in Fig. 6(a). For reference, we have shown the XANES spectrum of the Cu species of the Cu/rGO and Cu/rGO-CB catalysts, also shown for comparison are the XANES spectral absorbance of Cu metal foil, Cu_2O and CuO. The effective reduction of Cu^{2+} ions to the metallic Cu valence state can be confirmed from the XANES spectra of Cu/rGO and Cu/rGO-CB, which have similar features with that of Cu metal foil, suggesting that CuO in these catalysts was reduced to Cu. In addition, the white line peak of Cu/rGO-CB was stronger than for the Cu/rGO sample, indicating that the charge transfer from Cu atoms to CB atoms occurs when adding the CB. The results also imply a strong interaction between the metal and support compared to those in the other catalysts. Fourier transforms (radial structure function, RSF) of Cu K-edge k^3-weighted extended X-ray absorption fine structure (EXAFS) spectra of the supported Cu catalysts are presented in Fig. 6(b). The absorption peaks at 1.8–2.5 Å could be ascribed to the Cu-Cu bonds of Cu metal [56,57], the intensity of which decreased in the order of Cu/rGO > Cu/rGO-CB. Generally speaking, the intensity of this peak gradually increases with increasing average crystallite size of the corresponding metal species in the RSF [58]. The peak strength for the Cu-Cu bond represents the coordination number thereof, and the larger the coordination number, the larger the Cu crystallite size. The Cu/rGO catalyst had the largest Cu crystallite size, while the Cu/rGO-CB catalyst had the smallest, as confirmed by the XRD results. Furthermore, there were small Cu crystals in the Cu/rGO-CB catalyst, suggesting high Cu dispersion and more active Cu sites, thus enhancing its catalytic performance.

3.1.6. SEM

The SEM images of GO, rGO, Cu/rGO, rGO-CB and Cu/rGO-CB are shown in Fig. 7. After the strong oxidation of GO shown in Fig. 7(a), the lamellar structure of the original compacted graphite is replaced by the fold and broken edge. When GO was reduced

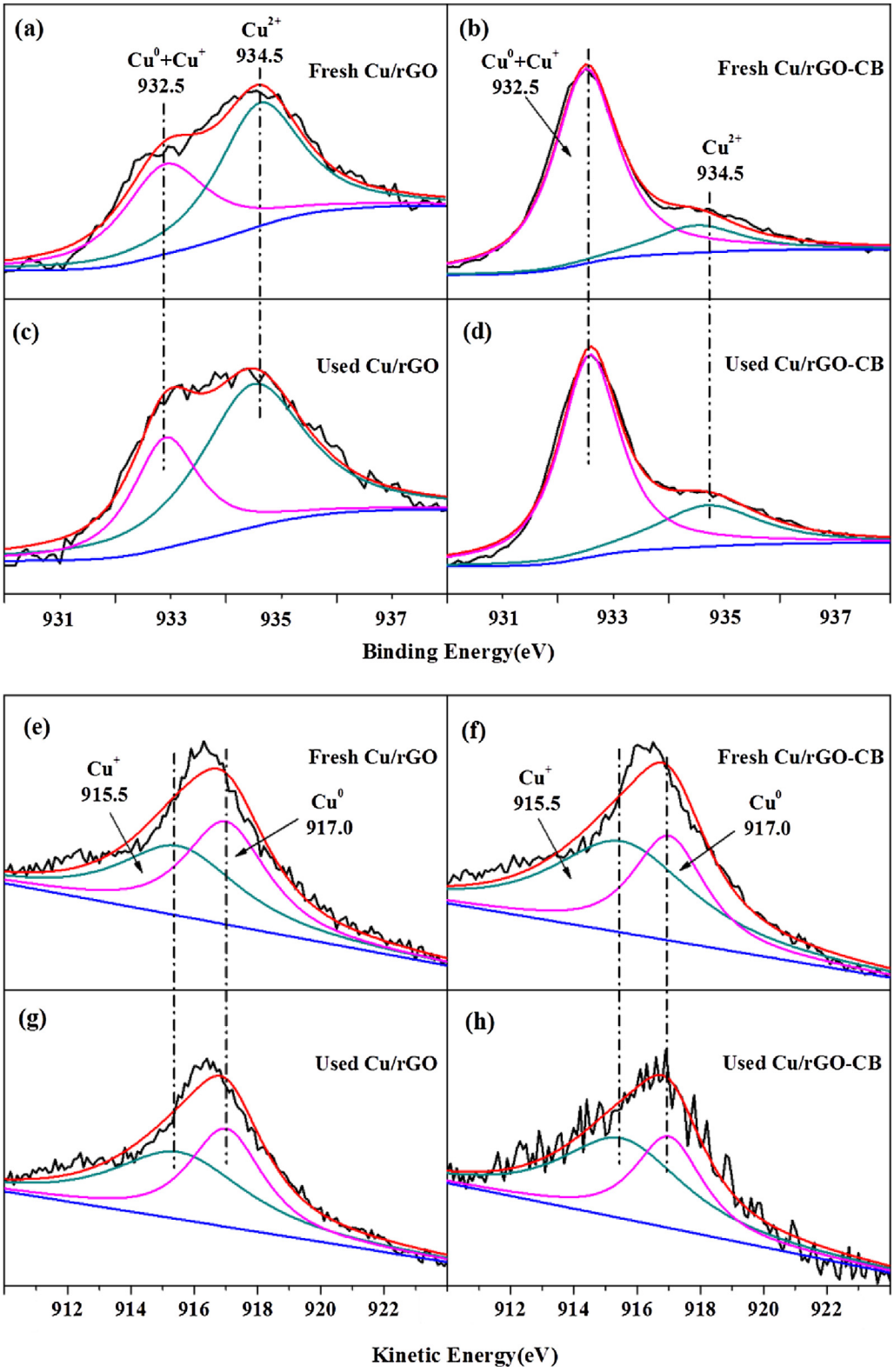

Fig. 5. XPS of Cu $2p_{3/2}$ (a–d) and the Cu LMM Auger (e–h) spectra of Fresh and Used Cu-based catalysts.

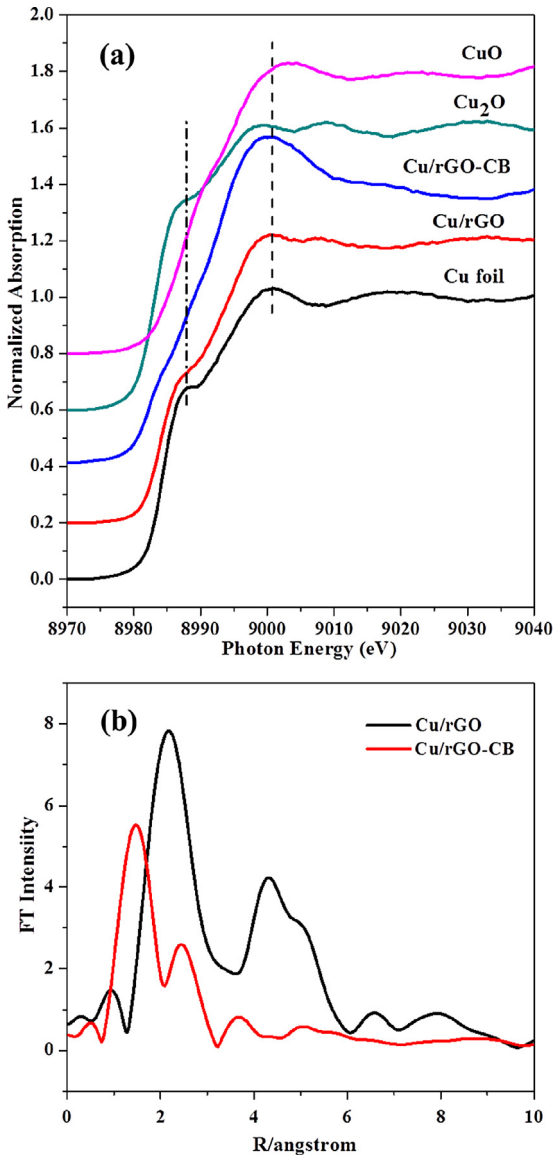

Fig. 6. The Cu K-edge XANES spectra of Cu foil, Cu_2O, CuO and Cu-based catalysts (a) and Fourier transforms of Cu K-edge k^3-weighted EXAFS of Cu/rGO and Cu/rGO-CB catalysts (b).

to rGO, the surface morphology changed significantly. It is obvious that for the rGO sheet without CB, the graphene layers were restacked together (Fig. 7(b)). As seen from the edge, a layered structure was presented, with the thickness of a layer of reduced graphene being about 20 nm, although the surface is covered with wrinkles, but very smooth. For the non-intercalated Cu/rGO catalyst, the agglomeration of graphene layers becomes more serious, which may be disadvantageous for the dispersion of Cu species (Fig. 7(c)). For the CB-intercalated rGO (Fig. 7(d)), it is observed that the rGO is not restacked together, which is mainly caused by the uniform distribution of the CB particles between the layers of rGO [28]. While for Cu/rGO-CB, the graphene layers were separated by CB (Fig. 7(e)), which will further increase the loading of Cu and facilitate Cu particle diffusion between graphene layers, owing to the expansion of surface area. This contributes to the higher activity of Cu/rGO-CB (see Section 3.2).

3.1.7. TEM

The distribution, morphology and size of NPs can be clearly observed in the TEM images. In Fig. 8(a), the irregularly wrinkled layers were obviously assigned to rGO, mainly because the graphene layers overlap in order to maintain thermodynamic stability. In addition, the structure of rGO was transparent, indicating that the GO film layer is relatively thin [59]. In the case of rGO intercalated with CB, as shown in Fig. 8(b), the CB particles are closely bonded to the surface of graphene sheets and the graphene surface is rough, indicating a strong interaction between CB particles and the rGO layer after undergoing the ultrasound and water bath heating process. However, the surface of rGO was no longer transparent, which may be caused by the adhesion of CB in the outer surface of graphene. The Cu/rGO catalyst also shows a similar flexible characteristic to the rGO film shown in Fig. 8(c). Particles with a uniform size of about 40 nm were randomly deposited on the large surface of rGO sheets. In the inset of Fig. 8(c), the higher solution TEM image shows well-defined lattice fringes having an interplanar spacing of 0.21 nm, which is in agreement with the (111) plane of cubic Cu [16]. This matches well with the XRD results. Fig. 8(d) presents the Cu/rGO patterns after a cyclic reaction for five times. Serious agglomeration of Cu NPs in some regions occurred and the particle size increased significantly, which may be because the flat and smooth surface of graphene is not conducive to the stable attachment of metal NPs. Furthermore, it caused serious deactivation of the catalyst. Fig. 8(e) shows a representative TEM image of the Cu/rGO-CB catalyst, which could enable better spatial distribution density of Cu nanocatalysts on the graphene intercalated with CB supports than the Cu/rGO. It known that the surface oxygenated groups of the support influence the dispersion of Cu species [15]. Intercalated CB can promote the stability of the metal NPs by electronic interaction with the support due to the rich oxygen nature of the CB surface [35]. From the particle size distribution, it can be determined that the average particle size of the Cu particles is 20 nm or less, which is mainly caused by the addition of CB, providing a broad space for the active metals. In addition, the Cu particles entering into the graphene layers are difficult to agglomerate in the spatial confinement effect, so the Cu particles are of a relatively small size. Fig. 8(f) shows the TEM spectra of Cu/rGO-CB after the reaction. The size of Cu NPs dispersed on the rGO-CB sheets is still about 20 nm, which further highlighted the advantage that doping CB can improve the dispersion and stability of the active component on the surface of the support. Obviously, the CB particles acted as a spacer to prevent the reunion of graphene sheets by the means of Van der Waals forces. Simultaneously, after CB was intercalated into rGO, the interaction between Cu and the support are distinctly increased, which is beneficial for the stability of the catalyst. The intercalated CB particles showed a three-dimensional composite structure, which was also beneficial to the promotion of the dispersion and stability of Cu particles.

3.1.8. CO-TPD

Various previous works have reported the reaction mechanism for DMC formation, it demonstrated that CO insertion to methoxide species is thought to be the rate-determining step of DMC formation [16,60–63]. Therefore, the catalytic performance is strongly dependent to the CO adsorption capability of the catalyst itself. The CO-TPD profiles of the Cu/rGO and Cu/rGO-CB are presented in Fig. 9. As depicted, Cu/rGO and Cu/rGO-CB show obvious and similar adsorption properties in the given TPD experimental conditions. As shown in Fig. 9, it is clear that the amount of CO adsorption for Cu/rGO-CB is larger than that of Cu/rGO, implying that Cu/rGO-CB possess more active sites, which is beneficial to the formation of DMC.

3.2. Oxidative carbonylation of methanol

Table 3 lists the catalytic performance of Cu/AC, Cu/CB, Cu/rGO and Cu/rGO-CB under the optimal reaction conditions for the

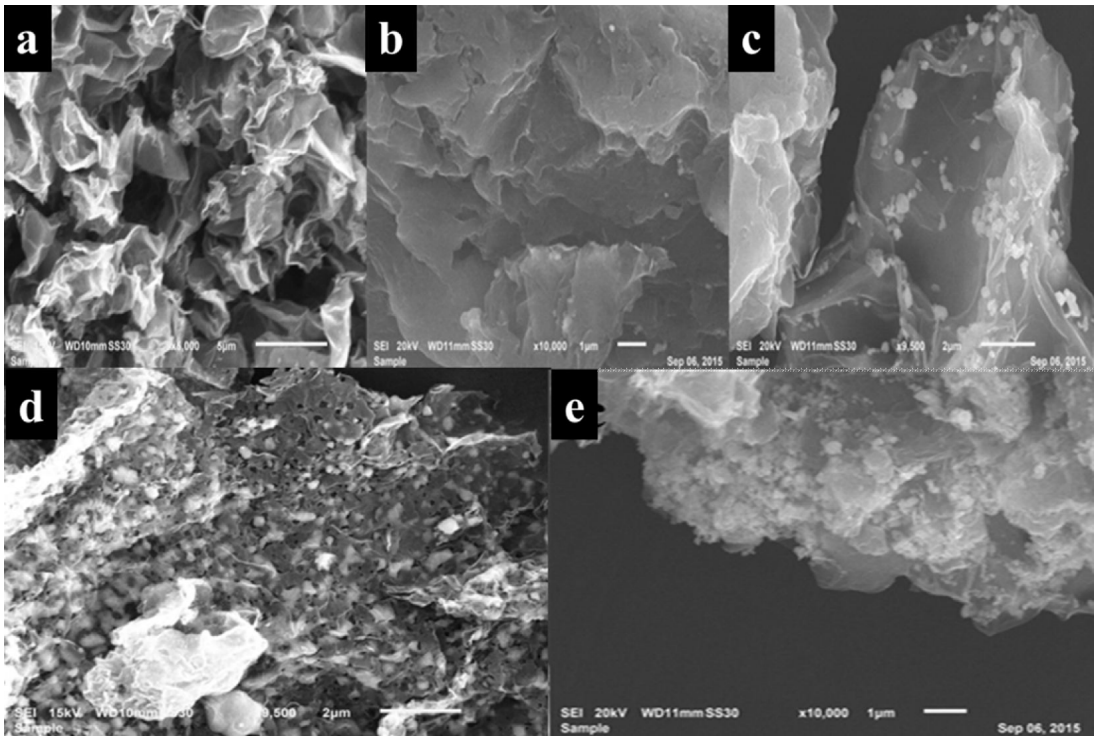

Fig. 7. SEM images of (a) GO, (b) rGO, (c) Cu/rGO, (d) rGO-CB and (e) Cu/rGO-CB.

Table 3
Catalytic activities of various catalysts[a].

Catalysts	C_{CH3OH}/%	S_{DMC}/%	S_{MF}/%	S_{DMM}/%	STY[b]/mg/(g h)
Cu/rGO	4.7	>99.9	–	–	2334
Cu/rGO-CB	5.6	97.4	3.6	–	2757
Regenerated Cu/rGO-CB	5.3	92.4	5.6	2.0	2641
Cu/CB	1.6	>99.9	–	–	809

[a] [Cu] = 16.69 mmol/L, P_{CO} = 2.0 MPa, P_{O2} = 1.0 MPa, t = 1.5 h, T = 120 °C.
[b] STY_{DMC} (mg/(g h)) = $m_{DMC}/(m_{cat}\cdot t)$.

liquid-phase oxidative carbonylation of methanol. It was clearly seen that the rGO-based catalysts are active for the DMC synthesis. The main byproducts of Cu/rGO-CB and Cu/AC catalysts are MF. The amount of carboxyl groups increased on the surface after the intercalation of CBs. It is reported that the direct interaction of the adsorbed methoxy species with the carboxyl groups could produce the MF [54]. Additionally, the Cu/rGO-CB and Cu/rGO catalysts were further tested to determine their catalytic stability. These catalysts all could be easily recovered through filtration and washing, then new substrates were added for the next cycle. Fig. 10 shows a summary of the obtained results. Obviously, the adding of CB particles leads to the higher activity (2757 mg/(g h)) and superior C_{CH3OH} than the pure graphene support supported Cu active center (2334 mg/(g h)). Furthermore, the catalytic activity of the Cu/rGO-CB catalyst indicated no significant decreases after five cycles (8.6%) than Cu/rGO (23.7%), suggesting that the catalytic stability of the Cu/rGO-CB is superior. Moreover, as shown in Table 3, the activity of used Cu/rGO-CB could be recovered to 95.8% of its initial level after it is reduced in 10 vol% H_2 (diluted with N_2), indicating that a slight oxidation of Cu nanoparticles occurs during the reaction. In addition, the deactivation of these catalysts is attributed to the loss and agglomeration of Cu species. As shown in Table 2, the Cu contents of catalysts were determined from XPS and AAS. The bulk Cu concentration of Cu/rGO is decreased by about 15.37%, from 6.57 to 5.56 wt.%. However, it is only decreased about 1.96% (from 7.12 to 6.98 wt.%) for the Cu/rGO-CB catalyst. In addition, the surface Cu concentration of both catalysts decreases by roughly the same amount.

This means that CB intercalated graphene composites can significantly improve the existence of Cu and further enhanced the activity and stability of the catalyst. In addition, compared to rGO, rGO-CB has more oxygen functional groups, which are beneficial for the catalytic activity and stability [37] (Fig. 5).

4. Conclusions

In summary, rGO supported Cu NPs catalysts were synthesized by conventional ultrasonication and a vacuum filtration method, and used for the synthesis of DMC via liquid-phase oxidative carbonylation of methanol. The effect of rGO intercalated by CB on the catalyst performance was also systematically investigated. Both the Cu/rGO and Cu/rGO-CB catalysts are active for the DMC synthesis, and the STY_{DMC} of 2334 and 2757 mg/(g·h) have been obtained, respectively. Based on the results of various characterization techniques, it can be concluded that the intercalation of CB particles into the layers of graphene leads to two positive effects. First, it can effectively prevent coalescence of graphene layers, and further increase the active surface area accessible for reactants to ensure

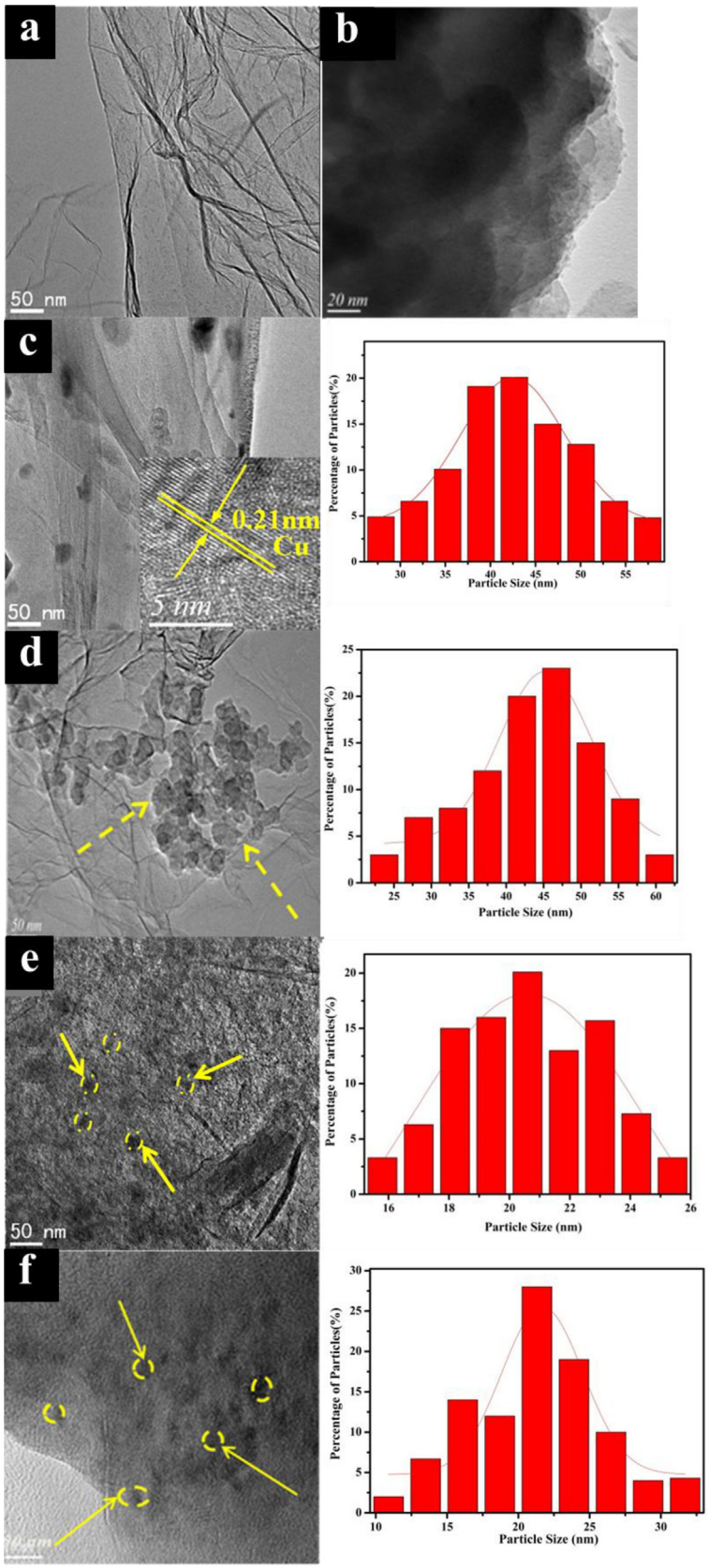

Fig. 8. TEM images of (a) rGO, (b) rGO-CB (c) Cu/rGO (d) Cu/rGO of after reaction, (e) Cu/rGO-CB and (f) Cu/rGO-CB of after reaction.

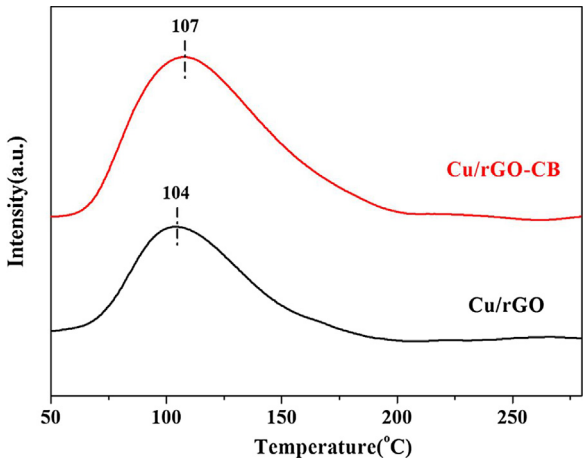

Fig. 9. CO-TPD patterns of the Cu/rGO and Cu/rGO-CB catalysts.

the Cu active sites can be efficiently utilized. Second, it is difficult to immobilize Cu NPs on graphene due to its smooth surface. However, CB contains abundant oxygen functional groups, which can enhance the stability of the metal NPs through the electronic interaction with metal NPs and further improve the catalyst stability. In addition, the catalyst was easily recycled by simple filtration and can be reused several times without a significant reduction in its catalytic activity. Even after five consecutive runs, the Cu/rGO-CB catalyst exhibited preferable catalytic activity and stability compared with Cu/rGO.

Acknowledgments

This work has been supported by a grant from the National Natural Science Foundation of China (21376159, 21606159 and 21776194) and Key Research and Development Program of Shanxi Province (201703D121022-1). The authors would like to thank Prof. Yongfeng Hu from Canadian Light Source for his help with XAFS analysis.

References

[1] H. Itoh, Y. Watanabe, K. Mori, H. Umino, Green Chem. 5 (2003) 558–562.
[2] M.A. Pacheco, C.L. Marshall, Energ. Fuel 11 (1997) 2–29.
[3] I. Sadaba, M. Lopez Granados, A. Riisager, E. Taarning, Green Chem. 17 (2015) 4133–4145.
[4] J. Zheng, J. Zhou, H. Lin, X. Duan, C.T. Williams, Y. Yuan, J. Phys, J. Phys. Chem. C 119 (2015) 13758–13766.
[5] I. Sadaba, M. Ojeda, R. Mariscal, M. Lopez Granados, Appl. Catal. B: Environ. 150 (2014) 421–431.
[6] H. Xiong, H.N. Pham, A.K. Datye, Green Chem. 16 (2014) 4627–4643.
[7] A. Zheng, C. Xia, Y. Xiang, M. Xin, B. Zhu, M. Lin, G. Xu, X. Shu, Catal. Commun. 45 (2014) 34–38.
[8] C.Z. Liu, F. Wang, A.R. Stiles, C. Guo, Appl. Energy 92 (2012) 406–414.
[9] J.S. Kruger, V. Nikolakis, D.G. Vlachos, Curr. Opin. Chem. Eng. 1 (2012) 312–320.
[10] W. Mo, H. Xiong, T. Li, X. Guo, G. Li, J. Mol. Catal. A: Chem. 247 (2006) 227–232.
[11] W.S. Dong, X. Zhou, C. Xin, C. Liu, Z. Liu, Appl. Catal. A: Gen. 334 (2008) 100–105.
[12] Y. Cao, J.C. Hu, P. Yang, W.L. Dai, K.N. Fan, Chem. Commun. (2003) 908–909.
[13] J. Ren, S. Liu, Z. Li, X. Lu, K. Xie, Appl. Catal. A: Ge (2017) n93–101.
[14] J.K. Nam, M.J. Choi, D.H. Cho, J.K. Suh, S.B. Kim, J. Mol Catal. A: Chem. 370 (2013) 7–13.
[15] G. Zhang, Z. Li, H. Zheng, T. Fu, Y. Ju, Y. Wang, Appl. Catal. B: Environ. 179 (2015) 95–105.
[16] M. Ren, J. Ren, P. Hao, J. Yang, D. Wang, Y. Pei, J. Lin, Z. Li, ChemCatChem 8 (2016) 861–871.
[17] P. Hao, J. Ren, L. Yang, Z. Qin, J. Lin, Z. Li, J. Chem. Eng. 283 (2016) 1295–1304.
[18] Y. Zhai, Z. Zhu, S. Dong, ChemCatChem 7 (2015) 2806–2815.
[19] Y. Hou, Z. Wen, S. Cui, S. Ci, S. Mao, J. Chen, Adv. Funct. Mater. 25 (2015) 872–882.
[20] A. Dandekar, R. Baker, M. Vannice, J. Catal. 183 (1999) 131–154.
[21] W. Wei, X. Qu, Small 8 (2012) 2138–2151.
[22] H. Zhao, Y.C. Lin, C.H. Yeh, H. Tian, Y.C. Chen, D. Xie, Y. Yang, K. Suenaga, T.L. Ren, P.W. Chiu, ACS Nano 8 (2014) 10766–10773.
[23] C. Ding, W. Wei, H. Sun, J. Ding, J. Ren, X. Qu, Carbon 79 (2014) 615–622.
[24] M.D. Stoller, S. Park, Y. Zhu, J. An, R.S. Ruoff, Nano Lett. 8 (2008) 3498–3502.
[25] B.F. Machado, P. Serp, Sci. Catal. Technol. 2 (2012) 54–75.
[26] J. Yan, T. Wei, B. Shao, F. Ma, Z. Fan, M. Zhang, C. Zheng, Y. Shang, W. Qian, F. Wei, Carbon 48 (2010) 1731–1737.
[27] Y. Yao, Q. Fu, Y. Zhang, X. Weng, H. Li, M. Chen, L. Jin, A. Dong, R. Mu, P. Jiang, L. Li, B. Hendrik, L. Zhi, S.B. Zhang, X. Bao, Proc. Natl. A Sci. 111 (2014) 17023–17028.
[28] Y. Wang, J. Chen, J. Cao, Y. Liu, Y. Zhou, J.-H. Ouyang, D. Jia, J. Power. Sources 271 (2014) 269–277.
[29] X. Dong, K. Wang, C. Zhao, X. Qian, S. Chen, Z. Li, H. Liu, S. Dou, J. Alloy Compd. 586 (2014) 745–753.
[30] Z. Wang, C. Ma, H. Wang, Z. Liu, Z. Hao, J. Alloy Compd. 552 (2013) 486–491.
[31] Y. Wang, C.X. Guo, X. Wang, C. Guan, H. Yang, K. Wang, C.M. Li, Energy Environ. Sci. 4 (2011) 195–200.
[32] H. Li, S. Pang, X. Feng, K. Müllen, C. Bubeck, Chem. Commun. 46 (2010) 6243–6245.

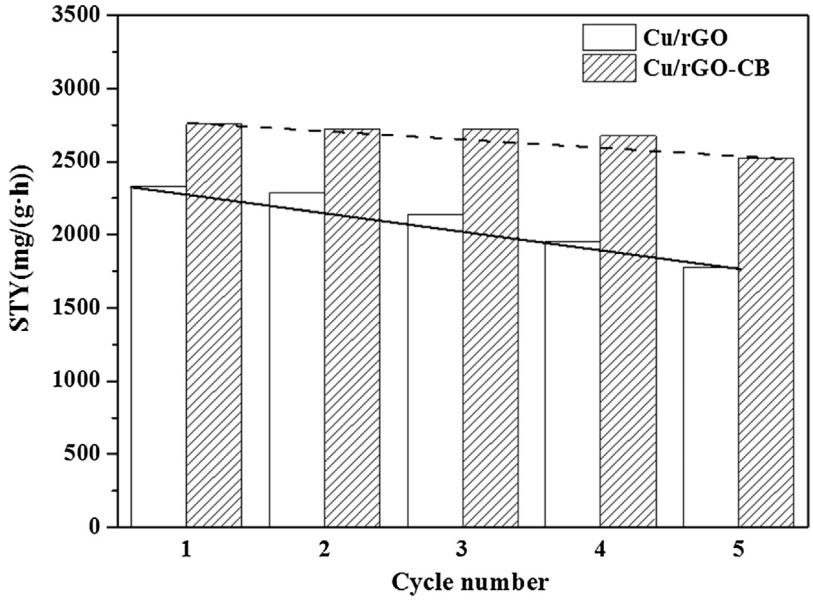

Fig. 10. Cycling performance of Cu/rGO and Cu/rGO-CB catalysts (Reaction conditions: P_{CO} = 2.0 MPa, P_{O2} = 1.0 MPa, t = 1.5 h, T = 120 °C).

[33] A.R. Siamaki, S.K. Abd El Rahman, V. Abdelsayed, M.S. El-Shall, B.F. Gupton, J. Catal. 279 (2011) 1–11.
[34] S. Sharma, A. Ganguly, P. Papakonstantinou, X. Miao, M. Li, J.L. Hutchison, M. Delichatsios, S. Ukleja, J. Phys. Chem. C 114 (2010) 19459–19466.
[35] Y. Li, Y. Yu, J.G. Wang, J. Song, Q. Li, M. Dong, C.J. Liu, Appl. Catal. B: Environ. 125 (2012) 189–196.
[36] Y. Li, Z. Zhou, G. Yu, W. Chen, Z. Chen, J. Phys. Chem. C 114 (2010) 6250–6254.
[37] S. Paul, E.E. Santiso, M.B. Nardelli, J. Phys.: Condens. Mat. 21 (2009) 355008.
[38] S.M. Paek, E. Yoo, I. Honma, Nano Lett. 9 (2008) 72–75.
[39] C. Hontoria-Lucas, A. Lopez-Peinado, J.d.D. López-González, M. Rojas-Cervantes, R. Martin-Aranda, Carbon 33 (1995) 1585–1592.
[40] G. Wang, J. Yang, J. Park, X. Gou, B. Wang, H. Liu, J. Yao, J. Phys. Chem C. 112 (2008) 8192–8195.
[41] R.L. Moss, D. Pope, B. Davis, D. Edwards, J. Catal. 58 (1979) 206–219.
[42] X.Y. Yan, X.L. Tong, Y.F. Zhang, X.D. Han, Y.Y. Wang, G.Q. Jin, Y. Qin, X.Y. Guo, Chem. Commun. 48 (2012) 1892–1894.
[43] A. Oberlin, P. Thrower, Chemistry and Physics of Carbon, vol. 22, Marcel Dekker New York, 1989.
[44] H.L. Guo, X.F. Wang, Q.Y. Qian, F.B. Wang, X.H. Xia, ACS Nano 3 (2009) 2653–2659.
[45] Y. Zhang, W. Hu, B. Li, C. Peng, C. Fan, Q. Huang, Nanotechnology 22 (2011) 345601.
[46] Z. Li, Y. Mi, X. Liu, S. Liu, S. Yang, J. Wang, J. Mater. Chem. 21 (2011) 14706–14711.
[47] S. Park, J. An, I. Jung, R.D. Piner, S.J. An, X. Li, A. Velamakanni, R.S. Ruoff, Nano Lett. 9 (2009) 1593–1597.
[48] E. Papirer, R. Lacroix, J.B. Donnet, G. Nanse, P. Fioux, Carbon 32 (1994) 1341–1358.
[49] E. Desimoni, G. Casella, A. Salvi, Carbon 30 (1992) 521–526.
[50] G. Merza, B. László, A. Oszkó, G. Pótári, K. Baán, A. Erdőhely, J. Mol Catal. A: Chem. 393 (2014) 117–124.
[51] X. Guo, C. Hao, G. Jin, H.Y. Zhu, X.Y. Guo, Angew. Chem. Int. Ed. 53 (2014) 1973–1977.
[52] B. Yan, S. Huang, S. Wang, X. Ma, Chemcatchem 6 (2015) 2671–2679.
[53] K. Shi, S. Huang, Z. Zhang, S. Wang, X. Ma, Chin. Chem. Lett. 28 (2017) 70–74.
[54] G. Merza, B. László, A. Oszkó, G. Pótári, E. Varga, A. Erdőhelyi, Catal. Lett. 145 (2015) 881–892.
[55] J. Ren, W. Wang, D. Wang, Z. Zuo, J. Lin, Z. Li, Appl. Catal. A: Gen. 472 (2014) 47–52.
[56] F. Pinakidou, E. Paloura, G. Matenoglou, P. Patsalas, Surf. Coat. Technol. 204 (2010) 1933–1936.
[57] T. Yamamoto, T. Tanaka, S. Suzuki, R. Kuma, K. Teramura, Y. Kou, T. Funabiki, S. Yoshida, Top. Catal. 18 (2002) 113–118.
[58] S. Takenaka, T. Shimizu, K. Otsuka, Int. J. Hydrogen. Energy 29 (2004) 1065–1073.
[59] D. Geng, Y. Chen, Y. Chen, Y. Li, R. Li, X. Sun, S. Ye, S. Knights, Energy. Environ. Sci. 4 (2011) 760–764.
[60] Y. Zhang, A.T. Bell, J. Catal. 255 (2008) 153–161.
[61] S.A. Anderson, T.W. Root, J. Catal. 217 (2003) 396–405.
[62] R. Zhang, L. Song, B. Wang, Z. Li, J. Comput. Chem. 33 (2012) 1101–1110.
[63] J. Ren, P. Hao, W. Sun, R.N. Shi, S.S. Liu, Chem. Eng. J. 382 (2017) 673–682.